

Article

# Blast Effects of a Shear Thickening Fluid-Based Stemming Material

Younghun Ko  and Kiseok Kwak \*

Department of Geotechnical Engineering Research, Korea Institute of Civil Engineering and Building Technology, 283 Goyang-daero, Ilsanseo-gu, Goyang-si 10223, Korea; younghunko@kict.re.kr

\* Correspondence: kskwak@kict.re.kr

**Abstract:** The Trauzl test is widely used to measure the explosive power of a substance by determining the volume increase produced by the detonation of a tested explosive charge in the cavity of a lead block with defined quality and size. In this study, the Trauzl lead block test and a high-speed 3D digital image correlation (3D-DIC) system were used to evaluate the effect of stemming on a blast hole. The blasting experiments were conducted with emulsion explosives. The stemming materials adopted in this study were sand, aggregate, and shear thickening fluid (STF)-based stemming materials. The results of the blasting experiments and numerical analysis showed that the expansion rate of the lead block was most affected by STF-based materials, followed by aggregates and sand stemming. Furthermore, the displacement and surface strain on the block were the highest in the experimental case using STF-based stemming materials. The STF-based stemming material developed in this study in open pit mining or various blasting constructions is expected to increase rock fragment efficiency, compared to that of general blasting stemming methods, and reduce blasting vibration by decreasing the amount of explosive per blast hole used for blasting.

**Keywords:** Trauzl test; 3D digital image correlation; shear thickening fluid; stemming; blasting experiment



**Citation:** Ko, Y.; Kwak, K. Blast Effects of a Shear Thickening Fluid-Based Stemming Material. *Mining* **2022**, *2*, 330–349. <https://doi.org/10.3390/mining2020018>

Academic Editor: Pablo Segarra

Received: 1 April 2022

Accepted: 28 May 2022

Published: 1 June 2022

**Publisher's Note:** MDPI stays neutral with regard to jurisdictional claims in published maps and institutional affiliations.



**Copyright:** © 2022 by the authors. Licensee MDPI, Basel, Switzerland. This article is an open access article distributed under the terms and conditions of the Creative Commons Attribution (CC BY) license (<https://creativecommons.org/licenses/by/4.0/>).

## 1. Introduction

The main objective of stemming is to increase rock fragmentation by enhancing the efficiency of the explosive energy generated by an explosive charge loaded in a blast hole. Another objective is to minimize the vibration and noise by reducing the amount of explosives used.

The most commonly used stemming materials in blast work sites are sand; in some sites, crushed stones, aggregates with smaller particle sizes, and rock fragments are used. According to Wang et al. [1], when suitable stemming was carried out in a blast site, the efficiency of the blast energy utilization was increased by over 300% compared with cases using no stemming or unsuitable stemming. Thus, stemming is required to obtain a robust confinement for the blast hole, and is essential for rock blasting. To this end, it is imperative to properly select stemming materials based on their properties, such as adhesive strength and frictional resistance, inside the blast hole. If a proper stemming material is used in a site, the loss of explosive energy inside the hole can be minimized during the blasting and the fragmentation of the target bedrock can be improved, as the preserved pressure can be efficiently spread to the surroundings. In this way, effective blasting can be performed using only a small amount of explosive charge and the blasting construction cost can also be reduced [2].

In general, the use of fluid as a stemming material inside a blast hole produces satisfactory blasting results. Zhu et al. [3] performed an AUTODYN numerical analysis with various stemming materials, including fluid (water), sand, and air, filled inside the space between the internal explosives and the hollow wall inside the blast hole, under dynamic loading (e.g., explosions). The results revealed that water generated the most extensive

crushing area and is the most appropriate medium for shock-wave transmission. However, cracks are generated when the tensile stress exceeds the maximum tensile strength of the rock. Moreover, the large load applied during this process can be attributed to the reflection and bubble pulse of the shock wave, due to the presence of water, causing deformation and displacement of the rock. In general, water expands under the overpressure of air, and this energy is transferred to the bedrock, which causes destruction and cracks. Subsequently, the high-pressure vapor is released through the cracks and contributes to the crack extension [4]. Thus, water is regarded as an excellent stemming material for blasting. However, the stemming shape of water cannot be easily maintained, presenting challenges for achieving a sealing state. Therefore, water can be applied in vertical blast holes, but cannot be easily utilized in horizontal blast holes, which are used in works such as tunnel blasting.

In this study, a shear thickening fluid (STF)-based stemming material was developed, which has an increased shearing strength for dynamic shock, and behaves similarly to water during shock-wave propagation. STF, as an intelligent material, is characterized by its reversible energy absorption behavior under impulse loading [5–8], and its remarkable energy absorption capacity through viscous dissipation during shear thickening [9–11] and compression thickening [12,13].

STF is a dense colloidal dispersion containing nanosized solid particles inside a carrier fluid [14]. Initially, the random distribution of particles in the dispersion emerges in an ordered form upon applying a shear force because the hydrodynamic forces surpass the repulsive forces acting between the interstitial spaces of the particles. This arrangement of particles constitutes the order–disorder theory, which was proposed by Hoffmann in 1972 [15]. As the shear rate increases, the increased hydrodynamic forces tend to squeeze out the fluid between the interstitial spaces, resulting in the formation of hydroclusters. This phenomenon constitutes a hydrocluster mechanism proposed by Brady and Bossis in 1985 [16]. These clusters are stress-bearing components and cause jamming of particles when further shearing forces are applied.

One of the key characteristics of shear thickening fluid (STF) is the behavior in which dynamic viscosity increases with applied shear stress. The effect of dilatancy occurs when closely packed particles are combined with enough fluid to fill the gaps between them. At low velocities, the fluid acts as a lubricant, and the dilatant material flows easily.

At higher velocities, the liquid is unable to fill the gaps created by the particles, and friction greatly increases, causing an increase in viscosity. STF is also non-Newtonian in nature in that its viscosity is dependent on shear rate or shear rate history. This behavior is one type of deviation from Newton's law and is controlled by factors such as particle size, shape, and distribution. Empirical studies have also shown that shear thickening effects vary with different concentrations of particles and additives, and the molecular chain of the additives [17].

Shear thickening is a reversible phenomenon governed by the power law model. In general, a non-Newtonian fluid is described using the power law model, expressed in Equations (1) and (2):

$$\tau = K \left( \frac{\partial \mu}{\partial y} \right)^n = K(\gamma)^n = \tau = K(\gamma)^{n-1} (\gamma)^1, \quad \tau = \mu_{\text{apparent}}(\gamma), \quad (1)$$

$$\mu_{\text{apparent}} = K(\gamma)^{n-1} \quad (2)$$

where  $\tau$  is the shear stress exerted by the fluid,  $K$  is the fluid viscosity,  $\mu$  is the shear deformation,  $y$  is the distance from the reference layer,  $\frac{\partial \mu}{\partial y}$  is the strain rate,  $n$  is the flow behavior index, and  $\mu_{\text{apparent}}$  is the apparent viscosity.

As shown in Figure 1, if  $n = 1$ , the fluid behaves like a Newtonian fluid and if  $0 < n < 1$ , the fluid exhibits shear thinning properties. Moreover, several dispersions and liquid polymers exhibit shear thinning behavior when the value of  $n$  lies between 0.3 and 0.7. However, this depends on the particle concentration and molecular weight of the carrier fluid. Figure 1 also explains the relationship between the shear stress and shear strain rate

of STF; the shear thickening effect of STF was demonstrated by the lower rate of increase in shear stress at the low shear-strain-rate regions and a higher rate of increase at the high shear-strain-rate values.

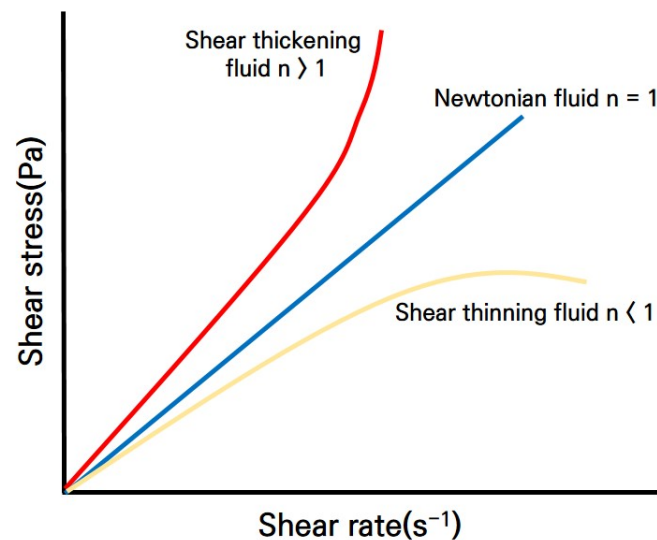


**Figure 1.** Schematic graph of the shear thickening mechanism of STF.

STF has been thoroughly researched in terms of its capability in enhancing the performance of body armor against ballistic impacts [18] and for stab resistance [19]. However, the potential effects of STF on the stemming of blast holes requires further investigation. The motivation herein is to harness the strength of the STF through flexible deployment and relatively easy stemming, while being able to dissipate pressure wave loading around the rock mass during an explosion. The rheological behavior of a non-Newtonian fluid is measured using a rheometer.

In this study, to comparatively analyze the blasting effect of the developed stemming material and that of commonly used blasting stemming materials, the Trauzl lead block test and numerical analysis were carried out. Furthermore, to measure the dynamic strain of the surface of the lead block during the blasting test, a 3D digital image correlation (3D-DIC) system was installed utilizing two high-speed cameras, and the expansion deformation of the lead block during the blasting process was measured.

## 2. Materials and Methods

### 2.1. Rheology Tests for STF-Based Stemming Material

The rheological tests were performed using a rheometer (Anton-Paar MCR301), and the STF samples were placed between a cone plate and the foundation support of the rheometer. The shear rate applied to the sample was raised from 0 to  $100 \text{ s}^{-1}$  during the experiments, and all the tests were conducted at a room temperature of  $25 \text{ }^\circ\text{C}$ . Figure 2a,b show the schematic of the rheometer and rheological test results of the STF-based stemming material, respectively.

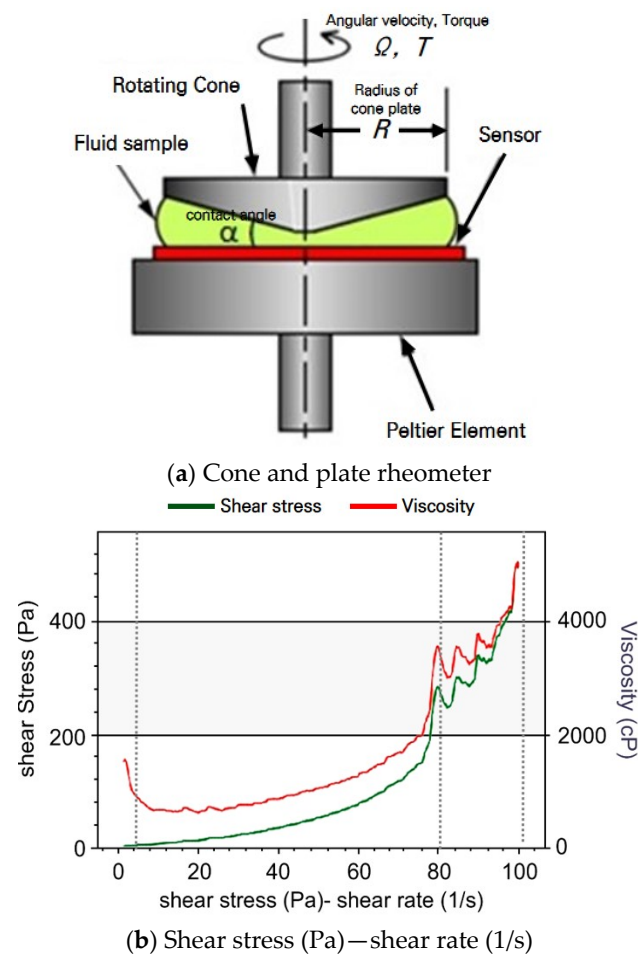


**Figure 2.** Cone and plate rheometer and rheological behavior results of STF-based stemming.

The experiments showed that a shear thickening effect was achieved at a critical shear rate of  $85 \text{ s}^{-1}$ . At first, a marginal shear-thinning of the STF samples was obtained, which subsequently increased with increasing shear rate. Specifically, as the shear rate attained a critical shear rate, the viscosity of the STF abruptly increased, which indicates the occurrence of the shear thickening phenomenon. However, the viscosity of the STFs sharply decreased after the period of shear thickening. The maximum viscosity of the STF samples was measured at 525 Pa.

## 2.2. Stemming Material

In general, sand or aggregate (gravel) is used as a stemming material for blasting. The stemming materials used for the Trauzl lead block blasting test in this study were sand, having an average diameter of 0.52 mm; gravels, having an average diameter of 2–3 mm; and STF-based stemming materials, as shown in Figure 3a–c. Figure 3d,e and Table 1 show the particle size distribution curves and the physical properties of the sand and the fine aggregate used in the experiment. In Table 1,  $D_{30}$ ,  $D_{60}$ , and  $D_{50}$  represent the size in mm in which 30%, 60%, and 50% of the particles are finer than the size represented, respectively.

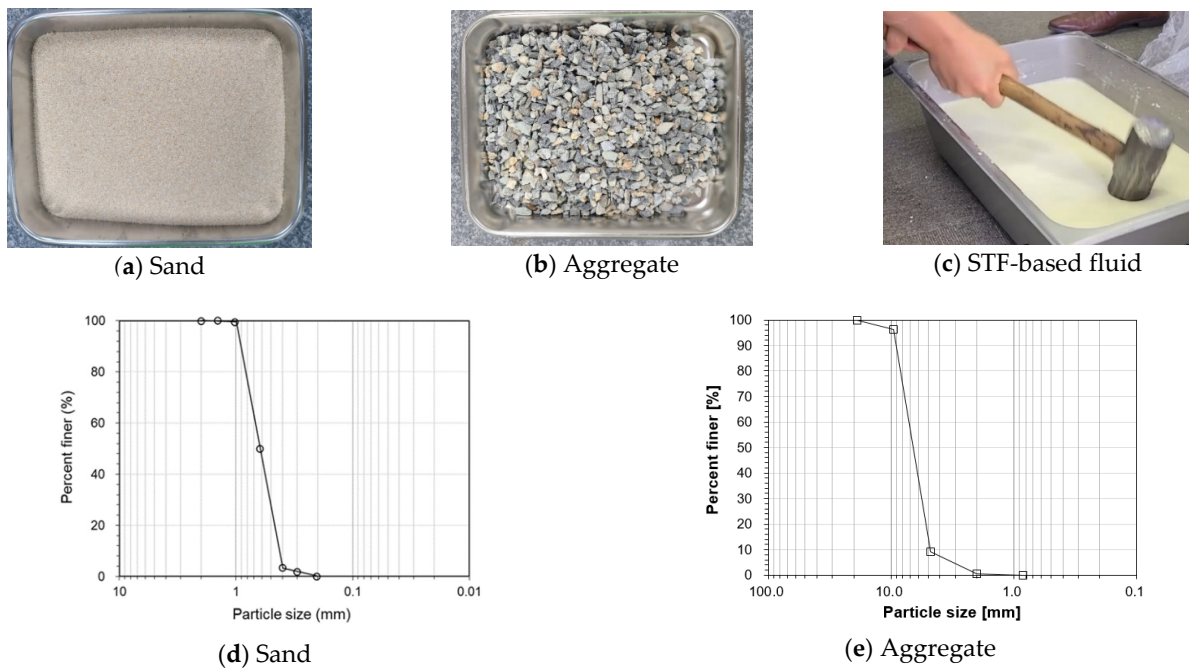


**Figure 3.** Stemming materials for Trauzl test and general stemming material particle size distributions.

**Table 1.** Properties of general stemming materials.

Type	D <sub>30</sub> (mm)	D <sub>60</sub> (mm)	D <sub>50</sub> (mm)	Uniformity Coeff. (C <sub>u</sub> )	Coeff. of Gradation (C <sub>c</sub> )	Specific Gravity (G <sub>s</sub> )	Unified Soil Classification System
Sand	0.52	0.7	0.62	1.35	1.14	2.65	poorly graded sand (SP)
Aggregate	5.5	7	6.5	1.45	0.90	2.45	poorly graded gravel (GP)

The sand used in the experiment corresponds to SP, and the aggregate corresponds to GP under the Korean standard classification. The fine aggregate is a finely ground crushed stone whose particles are thicker and coarser than those of sand, and thus have a superior frictional force. According to Jin [20], although crushed stones having a particle size ranging from 6 to 13 mm have excellent frictional force, the stemming effect may be reduced since the sealing capacity decreases in a blast hole with a short stemming length. Therefore, the particle size range was sieved to 2–3 mm in this experiment in order to maintain the sealing capacity of the aggregate stemming material.

The shear thickening fluid is comprised of cornstarch particles, with an approximate diameter of 5–20 μm, suspended in water. The STF was prepared at a concentration of 55 wt% and synthesized using a combination of mechanical and ultrasonic mixing. This weight fraction was selected to ensure the shear thickening behavior, while maintaining a workable solution [21]. According to previous experimental results [22], at 52.5–55 wt% of corn starch, a falling rock impacting on the suspension surface recoiled, similar to how it would behave after hitting a truly solid interface. Similarly, when the hammer in Figure 3c impacted on the STF suspension surface, the hammer recoiled.

In previous studies [12,13], the relationship between the shock velocity and viscosity for STF was obtained using laser-induced shock experiments. In addition, the STF acts as a solid after shear thickening, enabling the possible use of the Mie–Grüneisen equation of state (EoS) for describing the compressibility of STF.

As an example of the power series form for the Hugoniot, we can compute the power series expansion of the linear  $U_s - U_p$  Hugoniot. The relevant shock equations for STF

are mass, momentum conservation, and the assumed linear  $U_s - U_p$  relation, which are described in Equations (3)–(5), respectively:

$$\rho_0 U_s = \rho(U_s - u_p) \quad (3)$$

$$P_H = \rho U_s u_p \quad (4)$$

$$U_s = C_0 + S u_p \quad (5)$$

where  $U_s$  is the shock velocity in the  $U_s - U_p$  shock relationship, the constant  $C_0$  (bulk sound speed) is derived from least-square fits to experimental  $U_s - U_p$  data,  $S$  is the linear coefficient,  $U_p$  is the particle velocity,  $P_H$  is the pressure of the Hugoniot curve, and  $\rho_0$  is the density.

### 2.3. Trauzl Lead Block Test

The Trauzl lead block test, also called the Trauzl test or simply Trauzl, is a test used to measure the strength of explosive materials. The test is performed by loading a 10 g foil-wrapped sample of the explosive into a hole drilled in a lead block with specific dimensions and properties. The hole is then topped up with sand, and the sample is detonated electrically. After detonation, the increase in cavity volume is measured. The result, given in  $\text{cm}^3$ , is called the Trauzl number of the explosive.

The schematic of the lead block used in the experiment is shown in Figure 4. The height and diameter of the lead block were 200 mm, the central blast hole diameter was 25 mm, and the blast hole length was 125 mm. After the emulsion explosive (detonation velocity: 5664 m/s and density: 1.1~1.2  $\text{g}/\text{cm}^3$ ) was charged inside the bottom of the blast hole of the lead block, sand, aggregate, and STF-based materials were filled in the remaining space with the stemming material of the blast hole.

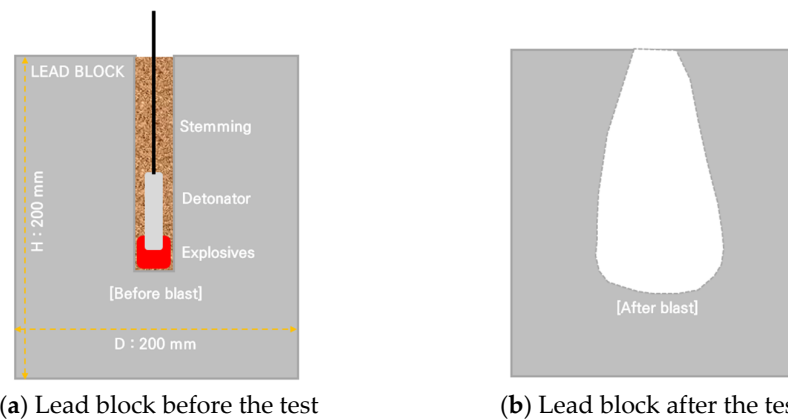


**Figure 4.** Schematic of the Trauzl test.

### 2.4. Preparation of the Experiments (Three-Dimensional High-Speed Camera System)

The experimental results were evaluated using two high-speed cameras and the DIC technique, and the expansion of the lead block after the initial explosion was recorded and analyzed. The DIC technique (Figure 5) was used to compare images before and after the deformation of a lead block, and to measure the displacement and strain rate of the entire surface. In recent years, some studies have applied this technique to blast engineering research. DIC has been applied in indoor tests to perform dynamic response analysis of the surrounding bedrock under different blast hole stemming conditions [23], and Xu et al. [24] analyzed the crack propagation characteristics of a cylindrical concrete specimen under blasting load during the crack propagation process using a stereo system comprising a high-speed camera and a 3D-DIC technique. Camera-based contactless precise displacement measurement technology is expected to be applied to blasting tests where it is difficult to attach contactable sensors.

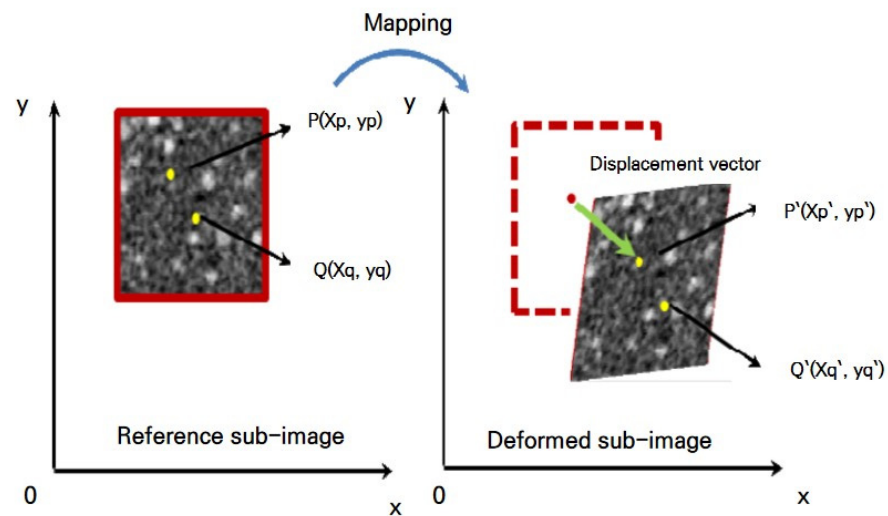


**Figure 5.** Schematic diagram for correlating the images of a reference subset before deformation and a target (or deformed) subset after deformation.

In this study, to measure the dynamic expansion process after the blasting of the lead block, two APX RS high-speed cameras manufactured by Photron were set up at 12,000 fps, as presented in Figure 6a. The distance to the lead block was 2.5 m, the distance between the two cameras was 1.0 m, and the entire area of the region of interest (ROI) for the image correlation was set at  $860 \times 860 \text{ mm}^2$ . To use the recording speed of 12,000 fps, an effective pixel area of only  $512 \times 384$  pixels was used, compared to the actual measurement area of  $430 \times 322 \text{ mm}^2$ . Table 2 provides a comparison of 2D/3D digital image correlation techniques.

Based on the singularity change in the speckle pattern, displacement or deformation can be more precisely measured. To easily recognize the travel path as an image, a black speckle pattern on a white background was spread onto the surface of the lead block (Figure 6b). This allowed for easy recognition of the dynamic expansion process and the surface change path of the lead block as images after the detonation of the explosive charge inside the explosive chamber of the lead block. Information on the grey-intensity change should be provided for the surface deformation of the evaluation target to be measured, which is necessary for proper reflection of the evaluation algorithm. To achieve this, an artificial random pattern is generally formed on the surface of the object of the analysis.

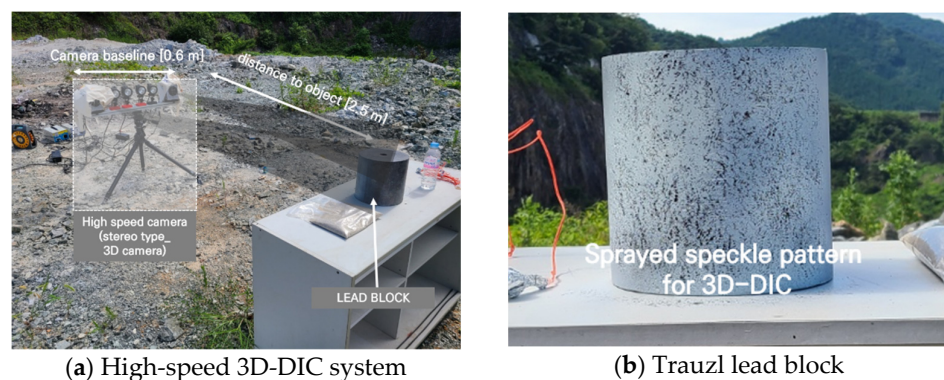


**Figure 6.** Installation of high-speed 3D-DIC system and Trauzl lead block.

**Table 2.** Comparison of 2D/3D image correlation systems.

	2D-DIC	3D-DIC
Number of cameras	Only 1	2 or more
Camera system	Mono	Stereo
Camera calibration	Not required	3D calibration
Measurement result	In-plane displacement (2D)	In-plane and out-of-plane displacement (3D)
Applications	Tensile test, bending test, shear test	Applicable to all experiments

2.5. AUTODYN Numerical Analysis

To simulate the lead block expansion test according to the application of the sand and fine aggregate stemming, numerical analysis was performed using AUTODYN. For this analysis, the physical properties of lead, sand, and aggregate were obtained based on the material library data of the AUTODYN program.

The equation of state (EoS) of ideal gas was applied for air, and the impact state equation was applied for other materials. The EoS is used to determine the volume and shape change in a material under different external loads, and different constitutive equations are applied depending on the state. Table 3 shows the physical properties of sand, fine aggregate, and STF, which are needed to use the EoS.

**Table 3.** Mie–Grüneisen EoS parameters for stemming materials.

Materials	Density D(g/cm <sup>3</sup> )	Sound Speed C <sub>0</sub> (m/s)	Coefficient S <sub>1</sub>	Coefficient S <sub>2</sub>	EoS
Sand	1.5	1019	1.32	0	shock
Aggregate	1.5	1100	1.40	0	shock
STF [12,13].	1.6	2050	5.32	0	shock
Lead	11.3	2006	1.43	0	shock

The lead block was composed of the three-dimensional Lagrange part, as presented in Figure 7; the stemming material and explosive charge inside the blast hole were composed of the Euler part, and Euler/Lagrange coupling 3D analyses were conducted. The explosive charge was set to be an emulsion charge using the physical properties shown in Table 4, and the Jones–Wilkins–Lee (JWL) model was applied. For the ambient condition of air, the internal energy was set to be  $2.068 \times 10^5$  J/kg, which corresponds to the standard atmospheric condition. The free boundary condition was applied at the borders of the lead block model, and the outflow condition was applied outside of the Euler region for the flow of the transferred gas.

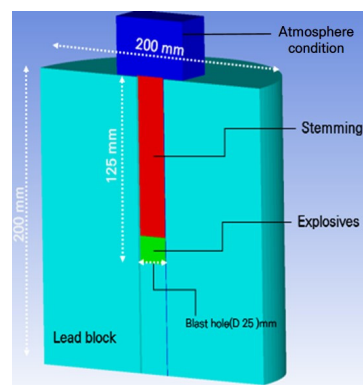


**Figure 7.** AUTODYN numerical model of the lead block.

**Table 4.** Jones–Wilkins–Lee (JWL) and Chapman–Jouguet (C-J) characteristic values (emulsion explosive [25]).

A(GPa)	B(GPa)	R1	R2	w
243	7.671	4.991	1.967	0.499

### 3. Experimental Results

For the STF-based blasting stemming material, sand, and fine aggregate, a total of six Trauzl lead block tests (two for each material) were carried out. Factors for the comparative evaluation of the stemming effect included the expansion rate of the lead block, the dynamic strain of the surface near the explosive chamber, and the change in the diameter of the cross-section near the explosive chamber. The experimental results were analyzed as shown in Table 5.

**Table 5.** Results of the Trauzl lead block test.

Test number	Stemming Material	Blast Hole Volume(cc) Before Blasting	After Blasting	Expansion Rate (Trauzl Number)	Average	Max Strain (%)	Section Displacement (Peak) at Bottom of Blast Hole (mm)
# 1	Sand	72	423	5.87	6.03	5.6	10.0
# 2		72	447	6.20		6.2	6.0
# 3	Aggregate	72	468	6.50	6.77	4.9	7.4
# 4		74	521	7.04		7.5	10.0
# 5	STF-based materials	72	527	7.32	7.12	7.5	11.0
# 6		72	506	7.03		7.1	10.2

As shown in Figure 8a, 368 data points were measured using a 3D-DIC system; these points were formed into a lead cylinder using a Gaussian best-fit technique to determine its diameter and cross-section. Figure 8b shows the process of forming the diameter and the cross-section near the chamber, starting from the lower surface of the test piece. The 3D-DIC technique identifies a random pattern created on the sample surface to measure the displacement. The strain is calculated by differentiating the displacement of the node element used in finite element analysis (FEM) and can be measured by the displacement of the entire region of the sample. In this experiment, a node element was created to calculate the strain, as shown in Figure 9.

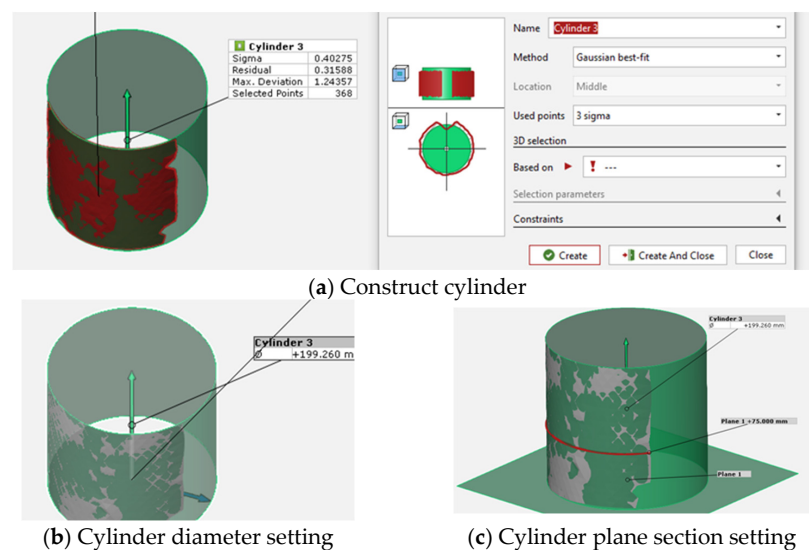


**Figure 8.** Construction of the fitting cylinder (lead block).

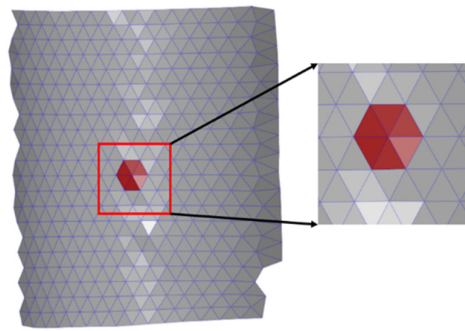


**Figure 9.** Calculation of the strain rate of the lead block using node element.

The initial volume of the lead block blast hole before the explosive charge detonation was measured to be 72–74 cm<sup>3</sup>, and the average expansion rate of the lead block after the explosion, i.e., the average Trauzl number, of the STF-based blasting stemming material was 7.12, higher than that of the fine aggregate (6.77) and sand (6.03). After estimating the blasting stemming effect of the STF-based stemming material based on the lead block expansion of the sand, the STF-based stemming material showed a stemming effect approximately 18% higher than that of sand. Table 6 shows the displacements of each designated point on the lead block surface measured using the 3D-DIC system, and these are the initial displacement data between the detonation of the explosive charge and the maximum expansion point of the lead block.

**Table 6.** Measurement points of high-speed 3D-DIC.

Point no.	Type of Displacement (mm)	After Detonation (ms)	Stemming Material								
			Sand			Aggregate			STF		
			0.25	0.5	1.0	0.25	0.5	1.0	0.25	0.5	1.0
# 1	Radius (coordinate displacement)		0.51	1.46	-	0.48	1.59	2.12	1.86	2.74	2.65
# 2			0.77	1.79	-	0.75	1.98	2.59	3.09	4.40	4.33
# 3			1.24	2.66	3.40	1.23	2.89	3.56	3.64	5.24	5.14
# 4			1.41	2.94	3.44	1.41	2.99	3.65	3.64	5.18	5.09
# 5			1.28	2.66	3.05	1.39	2.88	3.20	3.47	4.59	4.54
# 6			0.80	1.66	1.75	1.0	2.11	2.48	2.84	3.56	3.51
# 7			0.51	1.10	1.15	0.47	1.44	1.91	3.11	2.48	1.95
# 0	Section displacement (surface at the blasting chamber)		2.44	4.77	6.09	3.70	6.66	10.10	2.91	7.86	10.28

The 75 mm separation point from the bottom-center of the lead block is the explosive chamber surface where the explosive charges are charged. The displacement was calculated by designating points numbered 1–7 from the top of the block with 30 mm intervals, and the lead block was classified into three parts: upper, middle, and lower (Figure 10).

Figure 11 shows the change in the expansion of the lead block over time. For the cross-sectional displacement on the surface of the explosive chamber where the explosive charges are detonated, the STF stemming material showed approximately 1.6 times higher displacement compared to the sand at each time point, in addition to a slightly higher level of displacement compared with the fine aggregate (Figure 12). Figure 13 presents the average values of the displacements at points 3, 4, and 5 among the measurement points arranged in parallel on the lead block blast hole, and the STF stemming material showed a clearly higher radial displacement compared with that of sand and fine aggregate.

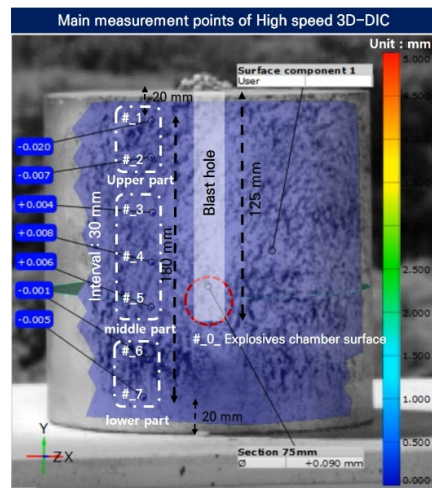


Figure 10. Schematic of measurement points of high-speed 3D-DIC.

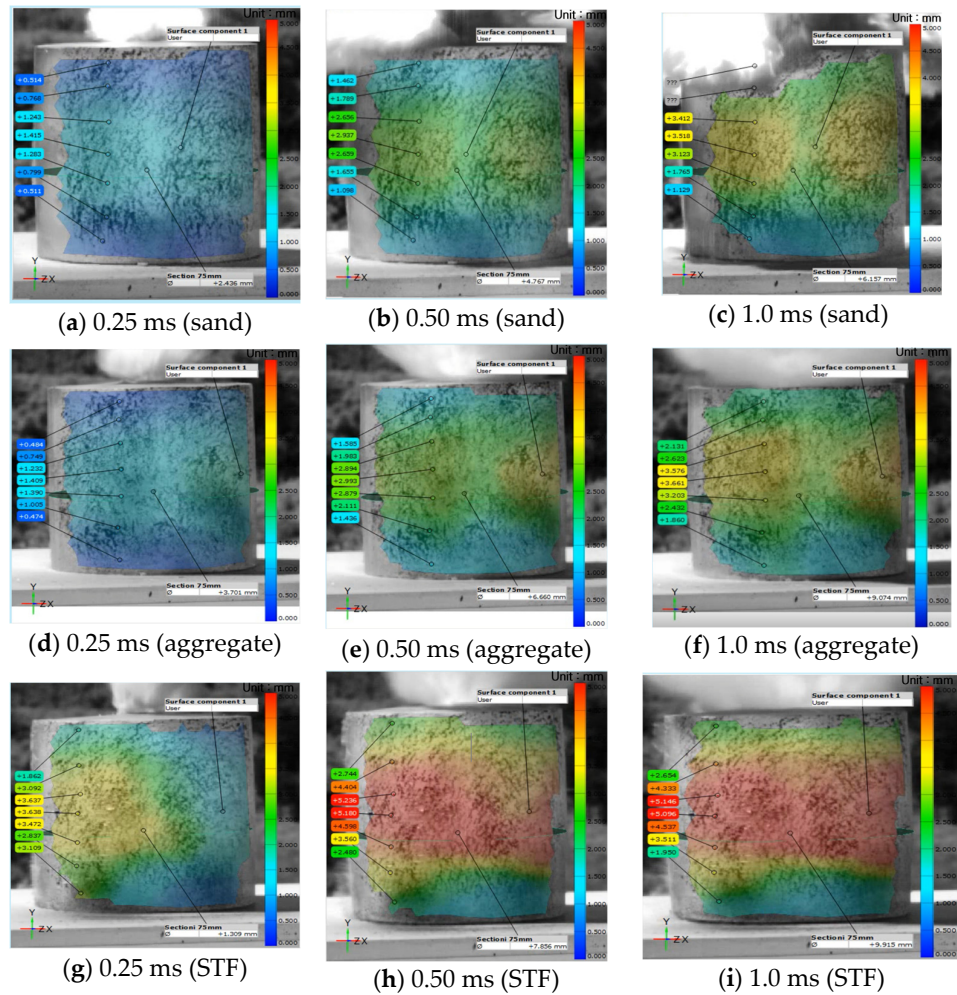
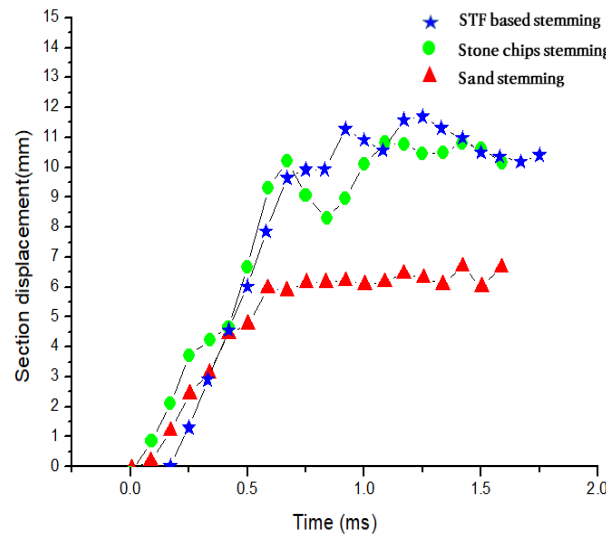
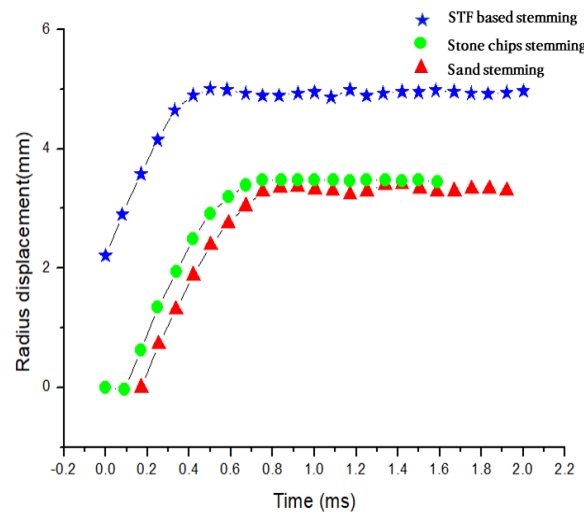


Figure 11. Surface displacement of the lead block after detonating.



**Figure 12.** Sectional displacement of the lead block at the surface of the explosive chamber with initial setting time after detonation.



**Figure 13.** Radial displacement of the lead block at the surface of the middle part with initial time after detonation.

Figure 14 presents the radial displacements at points 6 and 7, located at the bottom of the blast hole. The maximum radial displacement of the STF-stemming material was almost 1 mm higher than that of the fine aggregate and 1.5 mm higher than that of sand. A large displacement occurring at the bottom of a blast hole indicates an effective transmission of the explosive pressure to the lower part of the hole due to tamping. If tamping is successful in an actual bench blasting, additional work such as auxiliary drilling may become unnecessary. The shape and the volume of the lead block of the aggregate stemming material are slightly wider than those of the sand stemming material, showing a volume expansion of approximately 5% to 6% at the center. The volume expansion near the bottom of the lead block for the fine aggregate stemming material is expected to be 40% to 60% larger than that of the sand stemming material.

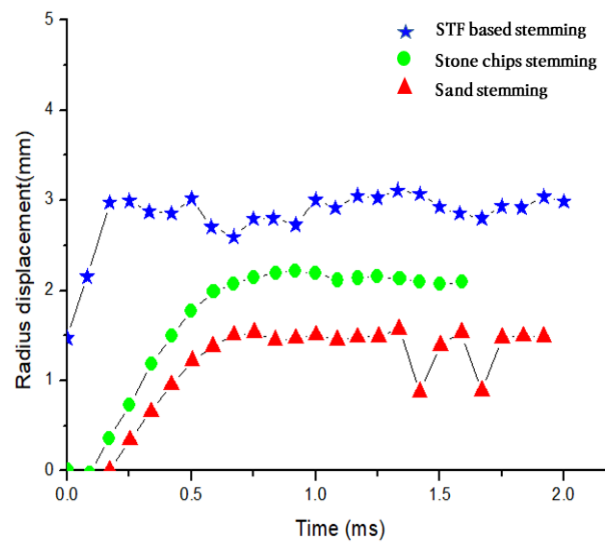


**Figure 14.** Radial displacement of the lead block at the surface of the lower blast hole with setting time after detonation.

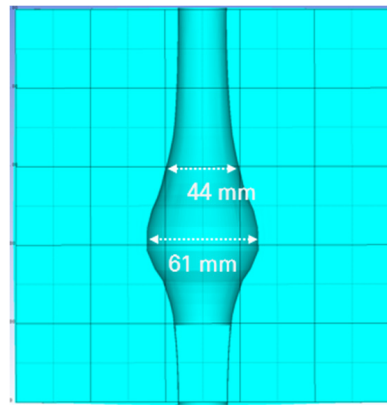
*Numerical Analysis Results*

The blast hole expansion results of the numerical model of the lead block expansion test for each stemming material are provided in Table 7. The initial volume of the lead block blast hole was 61 cm<sup>3</sup>, the expansion rate relative to the initial volume of the STF stemming was found to be 531%, and the Trauzl number of the STF stemming was higher than that of the sand stemming by approximately 1.0. Compared with the sand stemming case, the STF stemming showed an increase in the maximum expansion volume of around 24%. A comparison of the test results through numerical analysis yielded slight differences in the degrees of overall expansion of the lead block, although the trends of volume increase in sand stemming, aggregate stemming, and STF stemming were similar to those in the test results. The differences between the test results and numerical analysis are presumably due to errors in the casting process of the lead block, such as impurities and problems caused by the casting rate or casting temperature during production.

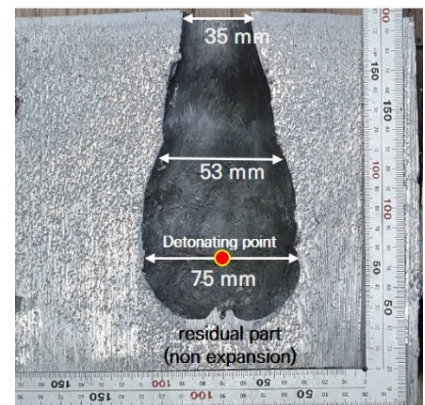
**Table 7.** Results for blast hole expansion of the AUTODYN lead block model.

Stemming Material	Sand	Aggregate	STF
Before blasting	61 cm <sup>3</sup>	61 cm <sup>3</sup>	61 cm <sup>3</sup>
After blasting	261 cm <sup>3</sup>	273 cm <sup>3</sup>	324 cm <sup>3</sup>
Expansion rate	427%	447%	531%

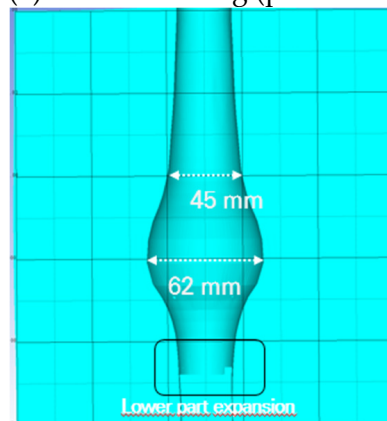
Figure 15 presents the expansion shape of the lead block blast hole with sand, fine aggregate, and STF stemming based on the experimental results and numerical analysis results. Clearly, the STF stemming resulted in the largest expansion diameter and showed additional expansion at the bottom of the blast hole. Figures 16–18 show the initial pressure distribution within the range of 0.1 to 0.15 ms after detonation. The pressure range in the left-hand figures ranged from 0 to 50 MPa. The pressure contour of the STF stemming was larger than that of the sand and fine aggregate.



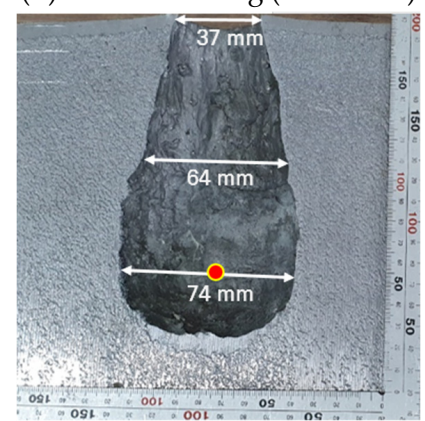
(a) Sand stemming (predicted)



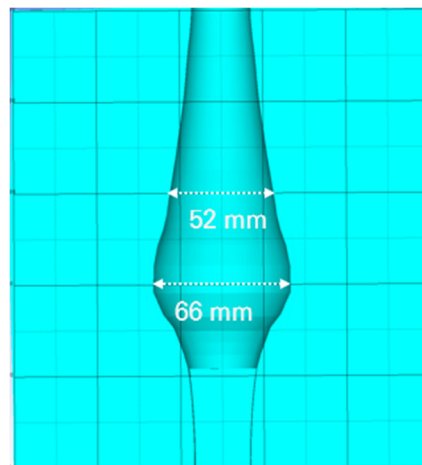
(b) Sand stemming (measured)



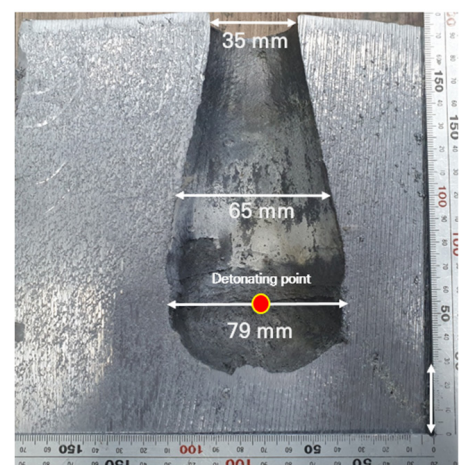
(c) Aggregate stemming (predicted)



(d) Aggregate stemming (measured)



(e) STF stemming (predicted)



(f) STF stemming (measured)

Figure 15. Blast hole expansion of the lead block according to different stemming materials.

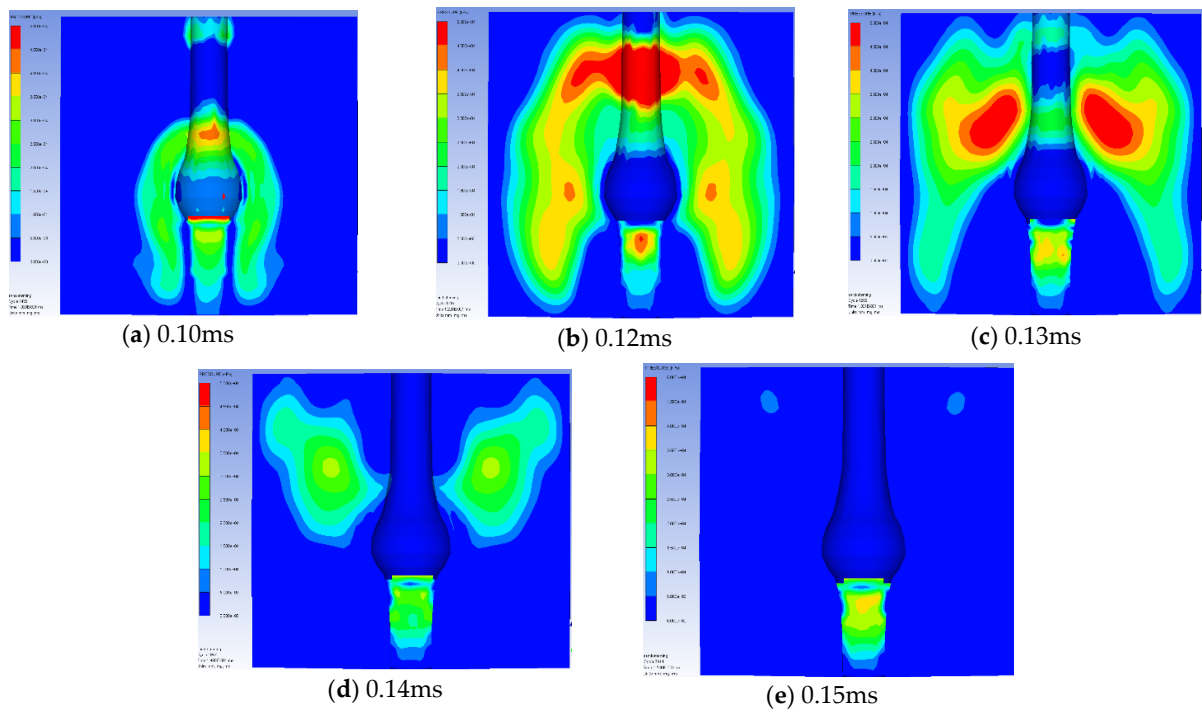


Figure 16. Pressure contour for the lead block model at the initial step (time: 0.1–0.15 ms; sand stemming cases).

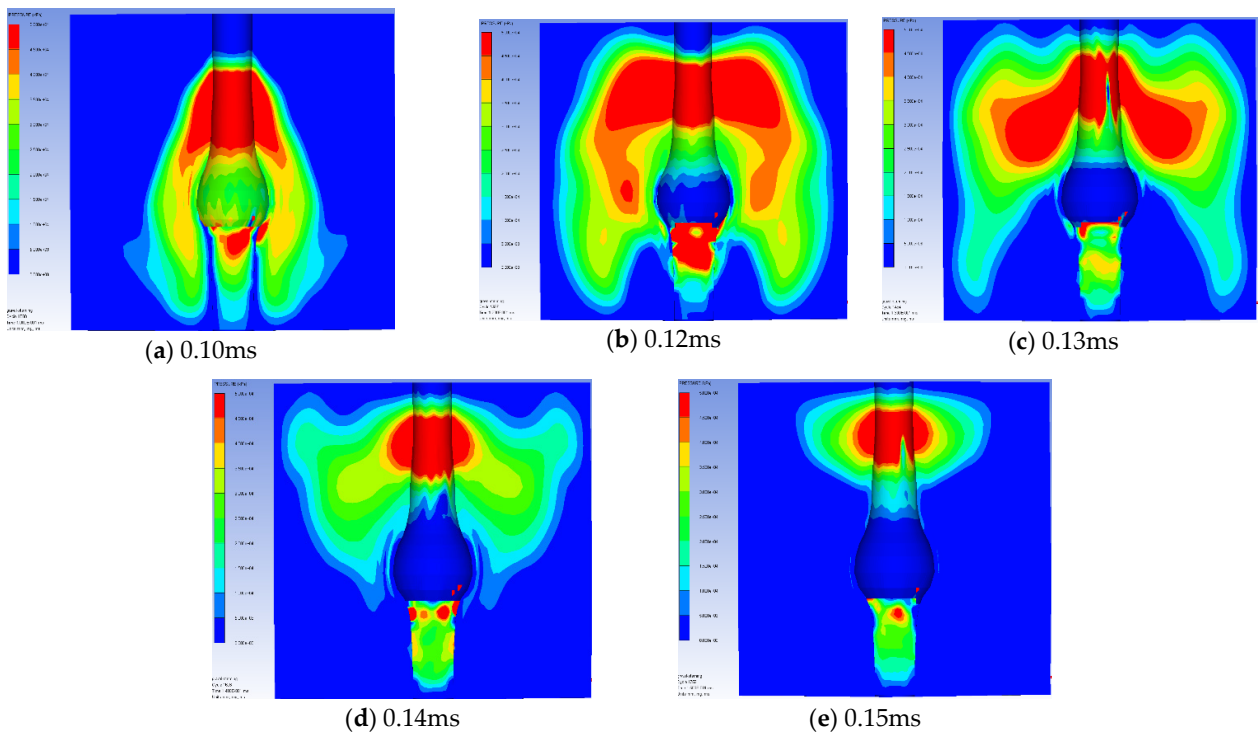


Figure 17. Pressure contour for the lead block model at the initial step (aggregate stemming cases).

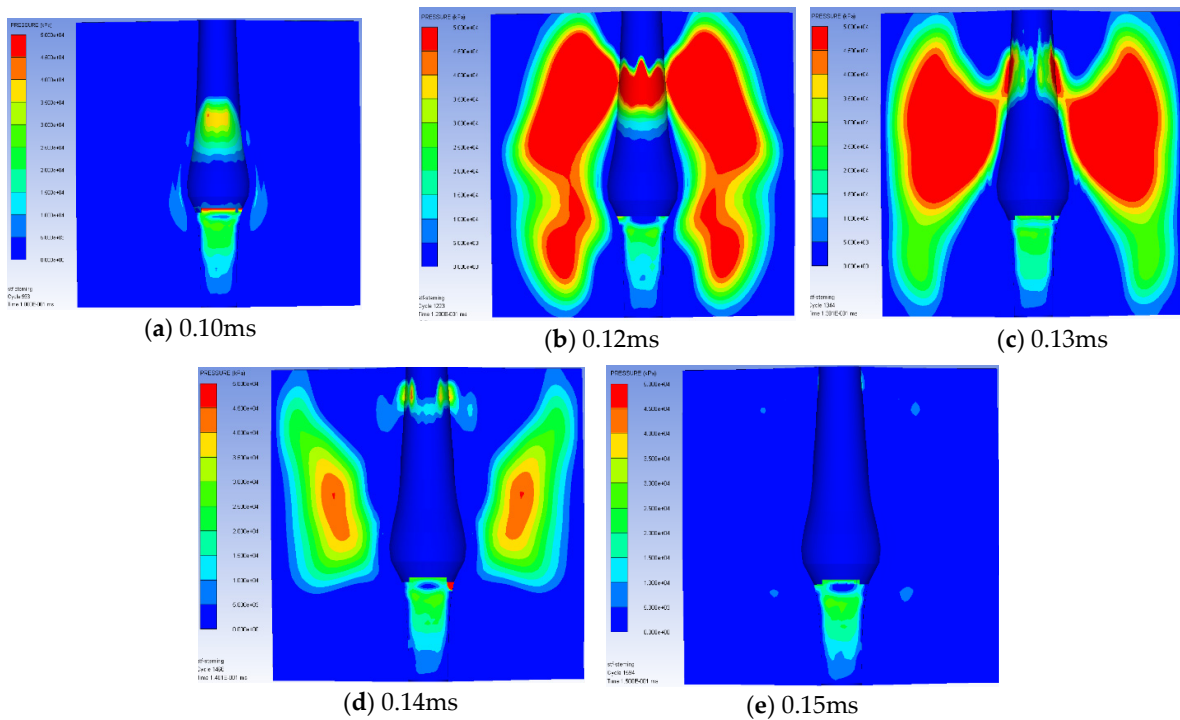


Figure 18. Pressure contour for the lead block model at the initial step (STF stemming cases).

Figure 19 shows a comparison of ejection times of the stemming materials. The ejection times for the sand and fine aggregate stemming were 0.45 ms (test result: 0.4 ms) and 0.75 ms (test result: 0.7 ms), respectively. The total ejection time of the STF stemming was 1.0 ms (test result: 0.9 ms), which indicated a significantly high ejection resistance concerning the blast borehole pressure. Hence, the STF stemming material has superior sealing capacity compared to general stemming materials such as sand and aggregate

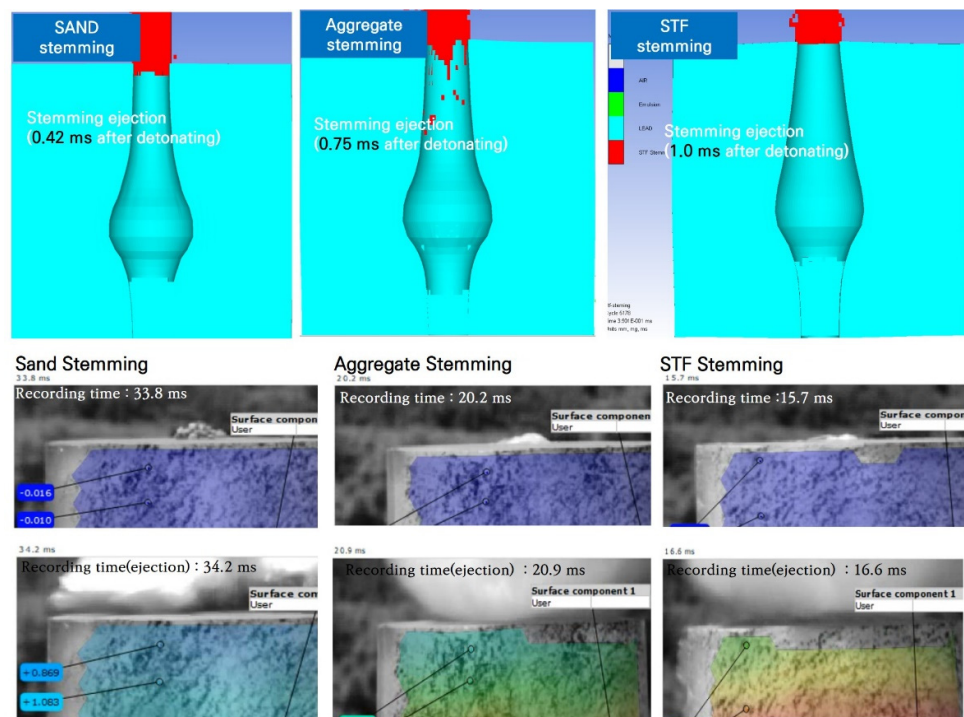


Figure 19. Stemming material ejection on the blast hole after detonating.

#### 4. Discussion

Figure 20 shows the comparative results of the Trauzl test and numerical analysis. Although there were some differences between numerical analysis and real experiments, the trends according to stemming materials were similar. The reason why the experimental and numerical analysis results are different is that the frictional resistance between the stemming part and blast hole wall was not considered in the numerical analysis, and the gas flow was not reflected in the analysis in detail.

The shock wave speed can be determined by the density of the material and Hugoniot slope,  $S$ , and bulk sound speed,  $C_0$ , in the shock relationship. In the case of STF, the density was slightly higher than that of sand and aggregate. However, the constants  $S$  and  $C_0$  were almost twice as high as those for sand or aggregate (Table 3). Therefore, it can be concluded that the lead block of STF expanded more than the sand and aggregate stemming cases because the shock wave speed generated was the highest in the case of STF.

Furthermore, the fluid medium (STF stemming) in the blast hole exhibits a favorable explosion transfer performance. The explosive detonation in the hole can produce highly uniform and wide damage to the surrounding rocks [26]. The impact of the high-intensity shock wave crushes the hard rock and forms compacted cavities in the soft rock [27].

The experimental lead block expanded more than that of sand and aggregate stemming, when the high-intensity pressure shock wave in the STF fluid stemming acted directly on the blast wall. Therefore, the superior blasting effect of STF stemming may be because of an effective sealing effect, in addition to the favorable characteristics of the transmission of shock waves.

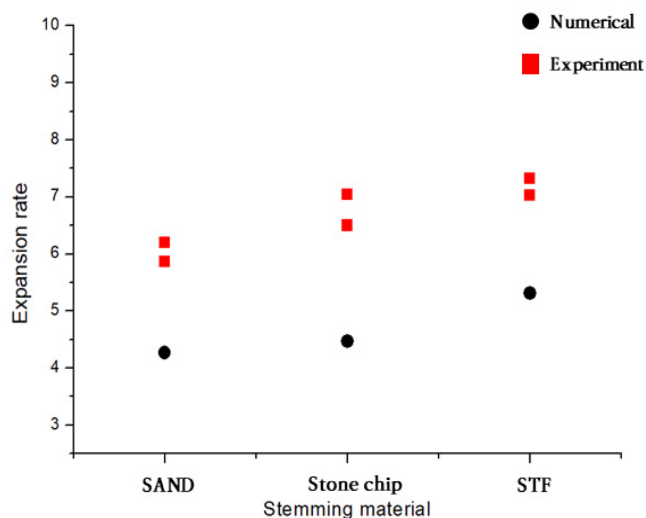
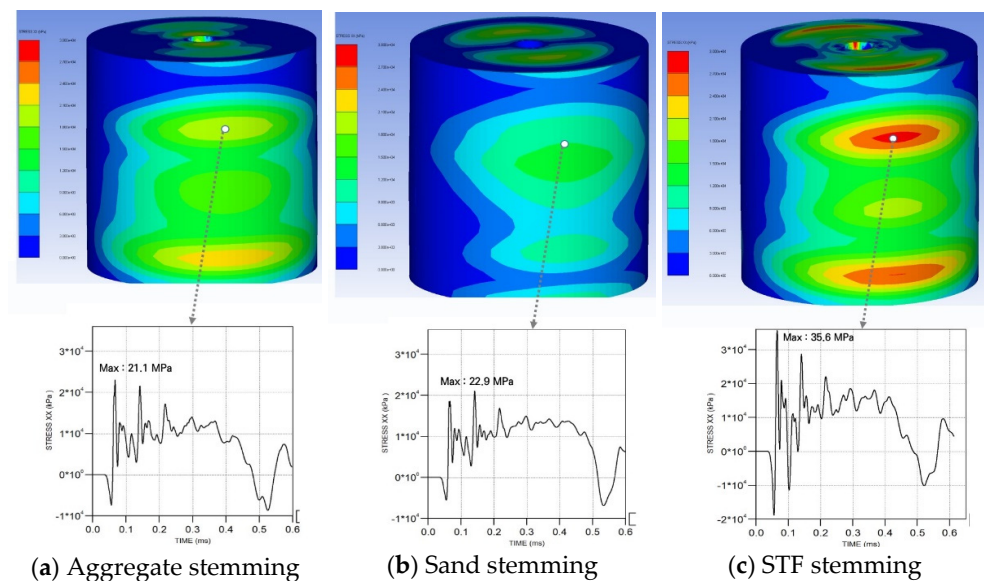


Figure 20. Comparison results graph of the Trauzl test and numerical analysis.

Figure 21 shows the stress ( $\sigma_{\chi\chi}$ ) on the surface of the lead block at 0.2 ms after blasting. In the time–stress curve at the specified point in Figure 21, the maximum stresses ( $\sigma_{\chi\chi}$ ) for the sand and fine aggregate stemming were 21.1 and 22.9 MPa, respectively.  $\sigma_{\chi\chi}$  of the STF stemming was 35.6 MPa. The significantly high stress resulting from the STF numerical model indicates that the block expanded more diametrically. Hence, the STF stemming material effectively and uniformly transmits explosion energy around the blast hole. Moreover, its stemming effect is superior to that of other stemming materials.



**Figure 21.** Stress ( $\sigma_{XX}$ ) contour on the surface of the lead block at 0.2 ms after blasting and the time–stress curve at the specified point.

## 5. Conclusions

In this study, experiments were performed to compare the stemming effects of two materials that are most commonly used for stemming at blasting sites with those of an advanced type of stemming material under material development. The results are summarized as follows.

- (1) Based on the results of the Trauzl lead block expansion test, the average Trauzl number of the shear thickening fluid-based stemming material was 7.12, indicating a higher average Trauzl number compared with that of sand stemming (6.03) and fine aggregate stemming (6.77). Furthermore, the developed STF stemming material showed a stemming effect enhanced by approximately 18% compared with that of sand.
- (2) In terms of the cross-section displacement on the surface of the explosive chamber of the lead block blast hole, the STF stemming showed approximately 1.6 times higher displacement compared with sand stemming, and it showed clearly higher radial displacement compared to sand and fine aggregate stemming at the measurement points arranged in parallel on the lead block blast hole at all locations, including the middle and lower parts of the blast hole.
- (3) According to the test results and numerical analysis, the STF stemming material effectively and uniformly transmits explosion energy near the blast hole. Moreover, its blast capacity is superior to that of other stemming materials, reducing the total specific charge. STF stemming is thus expected to be effective for the bottom cut of bench blasting.
- (4) Furthermore, both the test results and numerical analysis show that the STF stemming material lasted up to two times longer than sand in terms of ejection time. The STF stemming material applied in this study exhibited better sealing capacity than other stemming materials.
- (5) The superior blasting effect of STF stemming may be because of an effective sealing effect, in addition to the favorable characteristics of the transmission of shock waves. The STF-based stemming material developed in this study in various blasting constructions is expected to increase bedrock crushing efficiency, compared to that of general blasting stemming methods, and reduce blasting vibration by decreasing the number of explosive charges used for blasting.

**Author Contributions:** Writing—original draft preparation and review and editing, Y.K.; supervision and project administration, K.K. All authors have read and agreed to the published version of the manuscript.

**Funding:** This research was supported by a grant [22SCIP-C151438-04] from the Construction Technologies Program funded by the Ministry of Land, Infrastructure and Transport of the Korean Government. This research was supported by a grant from the project “Development of new stemming material and blasting method using shear thickening fluid by high shock-wave reaction,” which was funded by the Korea Institute of Civil Engineering and Building Technology (KICT).

**Conflicts of Interest:** The authors declare that there is no conflict of interest regarding the publication of this paper.

## References

1. Wang, J.; Chen, B. Theoretical discussion on optimization of blasting effect in surface mining. *Express Inf. Min. Ind.* **2005**, *24*, 19–21.
2. Ko, Y.H.; Kim, S.J.; Baluch, K.; Yang, H.S. Study on Blast Effects of Stemming Materials by Trauzl Lead Block Test and Numerical Analysis. *J. Korean Soc. Explos. Blast.* **2017**, *35*, 9–14.
3. Zhu, Z.; Xie, H.; Mohanty, B. Numerical investigation of blasting-induced damage in cylindrical rocks. *Int. J. Rock Mech. Min. Sci.* **2008**, *45*, 111–121. [[CrossRef](#)]
4. Bohlooli, B.; Gustafson, G.; Ronge, B. A laboratory study on reducing the quantity of rock fines at failure: Application to rock blasting and crushing. *Bull. Eng. Geol. Environ.* **2001**, *60*, 271–276. [[CrossRef](#)]
5. Jiang, W.; Gong, X.; Xuan, S. Stress pulse attenuation in shear thickening fluid. *Appl. Phys. Lett.* **2013**, *102*, 101901. [[CrossRef](#)]
6. Waitukaitis, S.R.; Jaeger, H.M. Impact-activated solidification of dense suspensions via dynamic jamming fronts. *Nature* **2012**, *487*, 205–209. [[CrossRef](#)]
7. Bender, J.; Wagner, N.J. Reversible shear thickening in monodisperse and bidisperse colloidal suspensions. *Rheology* **1996**, *40*, 899–916. [[CrossRef](#)]
8. Petel, O.E.; Hogan, J.D. An investigation of shear thickening fluids using ejecta analysis techniques. *Int. J. Impact Eng.* **2016**, *93*, 39–48. [[CrossRef](#)]
9. Newstein, M.C.; Wang, H.; Balsara, N.P.; Lefebvre, A.A.; Shnidman, Y.; Watanabe, H.; Osaki, K.; Shikata, T.; Niwa, H.; Morishima, Y. Microstructural changes in a colloidal liquid in the shear thinning and shear thickening regimes. *J. Chem. Phys.* **1999**, *111*, 4827–4838. [[CrossRef](#)]
10. Barnes, H.A. Shear-Thickening (“Dilatancy”) in Suspensions of Non aggregating Solid Particles Dispersed in Newtonian Liquids. *J. Rheol.* **1989**, *33*, 329–366. [[CrossRef](#)]
11. Laun, H.M.; Bung, R.; Hess, S.; Loose, W.; Hess, O.; Hahn, K.; Hädicke, E.; Hingmann, R.; Schmidt, F.; Lindner, P. Rheological and small angle neutron scattering investigation of shear-induced particle structures of concentrated polymer dispersions submitted to plane Poiseuille and Couette flow. *J. Rheol.* **1992**, *36*, 743. [[CrossRef](#)]
12. Wu, X.; Zhong, F.; Yin, Q.; Huang, C. Dynamic response of shear thickening fluid under laser induced shock. *Appl. Phys. Lett.* **2015**, *106*, 071903. [[CrossRef](#)]
13. Wu, X.; Yin, Q.; Huang, C. Experimental study on pressure, stress state, and temperature-dependent dynamic behavior of shear thickening fluid subjected to laser induced shock. *J. Appl. Phys.* **2015**, *118*, 173102. [[CrossRef](#)]
14. Boersma, W.H.; Laven, J.; Stein, H.N. Shear thickening (dilatancy) in concentrated dispersions. *AIChE J.* **1990**, *36*, 321–332. [[CrossRef](#)]
15. Hoffman, R.L. Discontinuous and Dilatant Viscosity Behavior in Concentrated Suspensions. I. Observation of a Flow Instability. *Trans. Soc. Rheol.* **1972**, *16*, 155–173. [[CrossRef](#)]
16. Brady, J.F.; Bossis, G. The rheology of concentrated suspensions of spheres in simple shear flow by numerical simulation. *J. Fluid Mech.* **1985**, *155*, 105–129. [[CrossRef](#)]
17. Xu, Y.; Gong, X.; Peng, C.; Sun, Y.; Jiang, W.; Zhang, Z. Shear Thickening Fluids Based on Additives with Different Concentrations and Molecular Chain Lengths. *Chin. J. Chem. Phys.* **2010**, *23*, 342–346. [[CrossRef](#)]
18. Lee, Y.S.; Wetzel, E.D.; Wagner, N.J. The Ballistic Impact Characteristics of Kevlar Woven Fabrics Impregnated with a Colloidal Shear Thickening Fluid. *J. Mater. Sci.* **2003**, *38*, 2825–2833. [[CrossRef](#)]
19. Decker, M.J.; Halbach, C.J.; Wetzel, E.D.; Nam, C.H.; Wagner, N.J. Stab Resistance of Shear Thickening Fluid (STF)-Treated Fabrics. *Compos. Sci. Technol.* **2007**, *67*, 565–578. [[CrossRef](#)]
20. Jin, Y.H. Study on the evaluation and selection of stemming materials for blasting demolition. Doctoral Dissertation, Chonnam National University, Gwang-Ju, Korea, 2017; pp. 15–20.
21. Bischoff White, E.E.; Chellamuthu, M.; Rothstein, J.P. Extensional rheology of a shear-thickening cornstarch and water suspension. *Rheol. Acta* **2010**, *49*, 119–129. [[CrossRef](#)]
22. Crawford, N.C.; Popp, L.B.; Johns, K.E.; Caire, L.M.; Peterson, B.N.; Liberatore, M.W. Shear thickening of corn starch suspensions: Does concentration matter. *J. Colloid Interface Sci.* **2013**, *396*, 83.e9. [[CrossRef](#)] [[PubMed](#)]

23. He, C.; Yang, J.; Yu, Q. Laboratory study on the dynamic response of rock under blast loading with active confining pressure. *Int. J. Rock Mech. Min. Sci.* **2018**, *102*, 101–108. [[CrossRef](#)]
24. Xu, Z.; Yang, J.; Guo, L. Study of the splitting crack propagation morphology using high-speed 3D DIC. *Explos. Shock. Waves* **2016**, *36*, 400–406.
25. Hansson, H. *Determination of Properties for Emulsion Explosives Using Cylinder Expansion Tests and Numerical Simulation*; Swedish Blasting Research Centre: Stockholm, Sweden, 2009; pp. 20–30.
26. Huang, B.; Li, P. Experimental Investigation on the Basic Law of the Fracture Spatial Morphology for Water Pressure Blasting in a Drillhole Under True Triaxial Stress. *Rock Mech. Rock Eng.* **2015**, *48*, 1699–1709. [[CrossRef](#)]
27. Yang, L.Y.; Ding, C.X. Fracture mechanism due to blast-imposed loading under high static stress conditions. *Int. J. Rock Mech. Min. Sci.* **2018**, *107*, 150–158. [[CrossRef](#)]